



1 **Muted orbital-scale Monsoon Variability over the Korean**
2 **Peninsula**

3 Nitesh Sinha^{1,2}, Axel Timmermann^{1,2}, Sun-Seon Lee^{1,2}, Kyoung-Nam Jo³, Jasper A. Wassenburg^{1,2}, Daniel
4 M. Cleary^{1,2}, Kyung-Sook Yun^{1,2}

5

6 ¹Center for Climate Physics, Institute for Basic Science, Busan, Republic of Korea

7 ²Pusan National University, Busan, Republic of Korea

8 ³Kangwon National University, Chuncheon, Gangwon-do, Republic of Korea

9

10 *Correspondence to:* Nitesh Sinha (nitesh@pusan.ac.kr)

11

12 **Abstract.** A recent study identified an east-west dipole pattern in East Asian Summer Monsoon
13 (EASM) variability in response to precessional-scale forcing (Wen et al., 2024). The Korean
14 Peninsula (KP) is situated near the nodal line of this dipole. It should therefore exhibit muted
15 precessional variability in precipitation and its oxygen isotope composition ($\delta^{18}\text{O}_p$). So far, this
16 conjecture has not been tested using paleoclimatic data. Here, we present speleothem $\delta^{18}\text{O}$
17 ($\delta^{18}\text{O}_{sp}$) records from the KP, which support the notion of suppressed orbital-scale
18 hydroclimate variability. Conducting a transient model simulation with the isotope-enabled
19 Community Earth System Model (iCESM) covering the past 130,000 years, along with tagging
20 experiments for low and high insolation conditions, we show that, on precessional scales,
21 isotopic contributions from oceanic and continental moisture sources compensate each other
22 over the KP, resulting in only a weak regional signal in $\delta^{18}\text{O}_p$. Based on iCESM1.2 simulations,
23 we further demonstrate that deuterium excess (d-excess) variability over the KP would still
24 capture the moisture source region's zonal seesaw response to precessional forcing, indicating
25 that the reconstruction of paleo water d-excess values from eastern Asian speleothem fluid
26 inclusions could provide new valuable insights into the drivers of regional monsoon systems.
27 This study provides new insights into the spatiotemporal variability of Pan-Asian
28 hydroclimates and its links to changes in moisture source.



29 **1 Introduction**

30 Speleothem (secondary carbonate deposits in caves) records, leveraged by radiometrically
31 constrained chronologies, have been a valuable resource for reconstructing paleo-hydroclimate
32 variability in tropical and subtropical regions (Braun et al., 2019; Cai et al., 2015; Cheng et al.,
33 2016; Gasse et al., 2011; Jo et al., 2017; Maher and Thompson, 2012). Such work is predicated
34 on stable oxygen-isotope ($\delta^{18}\text{O}$) measurements of speleothem calcite ($\delta^{18}\text{O}_{\text{sp}}$), which ultimately
35 derives from atmospheric moisture. When speleothem CaCO_3 precipitates under equilibrium
36 conditions, $\delta^{18}\text{O}_{\text{sp}}$ encodes cave air temperature and drip water $\delta^{18}\text{O}$. Drip water typically
37 reflects the $\delta^{18}\text{O}$ of precipitation ($\delta^{18}\text{O}_{\text{p}}$), integrating processes such as Rayleigh fractionation
38 along water-vapor pathways and, in some regions, the amount of regional rainfall (Lachniet,
39 2009). In regions where large changes in $\delta^{18}\text{O}_{\text{p}}$ are expected with respect to the effect of
40 temperature, $\delta^{18}\text{O}_{\text{sp}}$ is often considered as an indicator of atmospheric variability. Considering
41 $\delta^{18}\text{O}_{\text{sp}}$ as an indicator of atmospheric variability, $\delta^{18}\text{O}_{\text{sp}}$ -records from Chinese caves (e.g.,
42 Cheng et al., 2009; Wang et al., 2001) have provided key insights into seasonal and centennial-
43 to-orbital-scale variability in the Asian monsoon system. Speleothems that grew within the two
44 sub-monsoon branches of this system, the Indian Summer Monsoon (ISM) and the East Asian
45 Summer Monsoon (EASM), generally show a close correspondence in their $\delta^{18}\text{O}_{\text{sp}}$ variability
46 (Cai et al., 2015; Cheng et al., 2019; Kathayat et al., 2016), at least on orbital timescales. The
47 relationship was initially interpreted as an illustration of large-scale in-phase variations in
48 atmospheric processes across both monsoon systems (Cheng et al., 2009, 2016; Kathayat et al.,
49 2016; Wang et al., 2001). However, unlike the ISM, the EASM is characterized by more
50 complex spatial patterns in precipitation and in $\delta^{18}\text{O}_{\text{p}}$, even under present-day climate
51 conditions (Chiang et al., 2017; Wang et al., 2008; Zhao et al., 2012).

52 Our current understanding is that the EASM precipitation pattern is mainly driven by the



53 position of the subtropical front, which responds to Northern Hemispheric Summer Insolation
54 (NHSI). The frontal system, established through interactions between the Westerly jet and the
55 Western North Pacific Subtropical High (WNPSH), separates moist tropical air masses and
56 drier, colder extratropical air masses. The front is a primary rain-producing feature (Meiyu-
57 Baiu rainband, or Changma for the Korean Summer Monsoon) in the EASM (Chen and Chang,
58 1980; Ding, 2004; Wang et al., 2008), and it controls the seasonality (Hu et al., 2019; Liu et
59 al., 2022; Wang et al., 2008), rainfall distribution, intensity, and extent of the moisture
60 advection from tropical oceans (Lin et al., 2024; Volonté et al., 2022).

61 Speleothem-based studies, complemented by climate simulations, have reported a connection
62 between the EASM's characteristics (intensity and pattern) and frontal movements across
63 different timescales and under extreme climatic conditions (Chiang et al., 2015; Liu et al.,
64 2014; Volonté et al., 2022; Wang et al., 2008; Wu et al., 2018). For instance, Liu et al. (Liu et
65 al., 2014) demonstrate that frontal interactions with synoptic weather lead to heavier rainfall in
66 northern China during high NHSI (boreal summer perihelion conditions). Later, studies have
67 reported wetter conditions in central-eastern China or spatially opposite rainfall signals across
68 Asia during the last deglaciation (Termination I) in association with shifts in the position of the
69 Westerlies (He et al., 2021; Zhang et al., 2018). A recent study by Xue et al. (2025) proposed
70 that the intensity of the WNPSH played a key role in shaping hydrological conditions across
71 central China at various timescales.

72 On precessional timescales, a significant correlation between variability in Chinese $\delta^{18}\text{O}_{\text{sp}}$ and
73 NHSI implies a dominant control of the latter on the EASM, as the former has been interpreted
74 as an indicator of recorded changes in the EASM (Cai et al., 2015; Cheng et al., 2016; Kathayat
75 et al., 2016; Wang et al., 2001). This interpretation has, however, been challenged by other
76 regional precipitation-based proxies (Beck et al., 2018; Clemens et al., 2018; Sun et al., 2006;



77 Zheng et al., 2022) (e.g., loess magnetic susceptibility, seawater $\delta^{18}\text{O}$), which show only a weak
78 correspondence with the precessional cycle. Cheng et al. (2021) addressed the discrepancies
79 and complexities of hydroclimate proxies in Eastern Asia, explaining that loess, marine, and
80 cave records are complementary and preferentially capture specific aspects of Asian monsoon
81 dynamics. Further supported by Li et al. (2024), who found that the ratio of
82 dithionite–citrate–bicarbonate extractable iron to total iron in Chinese loess deposits
83 potentially records precipitation cycles on precessional scales. However, uncertainties in
84 interpreting the magnetic-susceptibility-based reconstructions remain, as they might reflect a
85 smoothed precipitation signal or be dominated by other forcings (Cheng et al., 2021; Sun and
86 Huang, 2006).

87 Isotope-enabled modeling offers an opportunity to further evaluate the roles of atmospheric,
88 land, and oceanic processes in a changing climate (i.e., transient simulations). They can help
89 interpret precipitation-based proxies by tracing the stable isotopologues of water
90 spatiotemporally (Battisti et al., 2014; Bosmans et al., 2018; Brady et al., 2019; Cheng et al.,
91 2021). Previous isotope modeling studies have discussed the complex relationship between
92 orbital-scale EASM $\delta^{18}\text{O}_p$ variability, NHSI, rainy seasons, and regional circulation patterns
93 (Dai et al., 2021; Liu et al., 2022; Yang et al., 2024). Though the major features of simulated
94 climate-isotopic signals across southern and eastern Asia agree with Chinese speleothem
95 isotope records, some models suggest a pronounced out-of-phase precipitation response
96 between the EASM rainband and the rest of the Asian monsoon on orbital timescales (Bosmans
97 et al., 2018; Hu et al., 2019). Isotope-enabled climate models also reveal large-scale differences
98 in the response of $\delta^{18}\text{O}_p$ to precessional forcing across Asia, with weaker anomalies over the
99 eastern domain than over the western domain (Battisti et al., 2014; Bosmans et al., 2018; Tabor
100 et al., 2018). A recent study elucidated the mechanisms underlying precession-scale EASM
101 precipitation and $\delta^{18}\text{O}_p$ variability and identified a grand dipole response pattern to orbital



102 forcing (Wen et al., 2024), which predicts weaker precessional variability over the nodal
103 regions, such as the Korean Peninsula (KP).

104 The KP lies at the boundary between northeast Asia and the Pacific, and moisture transport
105 through the WNPSH strongly controls summer precipitation variability over the region (Ha et
106 al., 2012; Wang and Lin, 2002). In the context of observed variations in $\delta^{18}\text{O}_p$, precipitation
107 isotope compositions in these areas may be influenced by various air masses and are primarily
108 determined by moisture sources (Araguás-Araguás et al., 1998; Jung et al., 2022; Kim et al.,
109 2019; Zhu et al., 2023). Studies have suggested that the moisture source predominantly drives
110 $\delta^{18}\text{O}_p$ over the KP, as inferred from the strong seasonality in deuterium excess (d-excess) in
111 present-day records (Lee, K.S. et al., 2001; Park, Y. et al., 2006). The seasonality of d-excess
112 is primarily attributed to oceanic airmass in summer (low d-excess) and the interaction between
113 a relatively warm oceanic airmass and a cold, dry continent air in winter (high d-excess)
114 (Yoshimura and Ichiyanagi, 2009).

115 While many studies (Clemens et al., 2018; Hayashi et al., 2017, 2021; Igarashi and Oba, 2006;
116 Iwamoto and Inouchi, 2007; Wen et al., 2024) have examined the eastern boundary of the
117 EASM system extensively, the KP has received less attention. We close this gap in our study
118 by focusing on variations of $\delta^{18}\text{O}$ ($\delta^{18}\text{O}_{sp}$ and $\delta^{18}\text{O}_p$) on the KP and the underlying mechanisms,
119 aiming to enhance our understanding of the pan-Asian monsoon system. Here, we explore the
120 dynamics by tracking and quantifying the moisture sources and their precessional modulation
121 of seasonal rainfall and isotopes over the KP. To this end, we consider new and previously
122 published $\delta^{18}\text{O}_{sp}$ records from two Korean stalagmites: ED1 (Eden Cave, (Jo et al., 2014)) and
123 GE1 (Gwaneum Cave, (Jo et al., 2010)). Moreover, to elucidate how large-scale changes in
124 circulation and moisture sources influence $\delta^{18}\text{O}_p$ variations over the KP on orbital timescales,
125 we conducted a series of transient climate and time-slice simulations and water-tagging



126 experiments. These simulations utilized the isotope-enabled Community Earth System Model
127 version 1.2 (iCESM1.2) and focused solely on the effect of orbital forcings. The transient
128 simulation with an orbital acceleration (Lorenz and Lohmann, 2004a) of 100 spans the past
129 130,000 years (130 ka). The iCESM1.2 time-slice simulations were conducted with fixed
130 minimum and maximum values of the precession index, reflecting northern hemisphere
131 summer perihelion and aphelion conditions, respectively. The results are further interpreted
132 using previously conducted high-resolution CESM1.2 simulations (Chu et al., 2020; Huang et
133 al., 2021; Raavi et al., 2023; Wengel et al., 2021) and a lower resolution transient CESM1.2
134 simulation, which includes orbital, greenhouse gas, and ice sheet forcings (Timmermann et al.,
135 2022; Yun et al., 2023).

136 **2 Materials and Methods**

137 **2.1 South Korean speleothem $\delta^{18}\text{O}_{\text{sp}}$**

138 We present $\delta^{18}\text{O}_{\text{sp}}$ records from two Korean stalagmites obtained from ED1 (Eden Cave (Jo et
139 al., 2014)) and GE1 (Gwaneum Cave (Jo et al., 2010)) (see locations in Fig. 1 and Fig. 2a),
140 which grew intermittently (Fig. S1). The $\delta^{18}\text{O}_{\text{sp}}$ records for ED1 and GE1 were previously
141 measured along with $\delta^{13}\text{C}_{\text{sp}}$ within the scope of Jo et al. (2010, 2014). However, the ED1 $\delta^{18}\text{O}_{\text{sp}}$
142 record remained unpublished to this date. The age models of these speleothems and the
143 associated $\delta^{13}\text{C}_{\text{sp}}$ records were previously discussed, and information on sampling and
144 measurement of stable isotopes can be found in Jo et al. (2010, 2014). Further details and the
145 periods covered by the $\delta^{18}\text{O}_{\text{sp}}$ records, as well as other proxies used in this study, are provided
146 in the supplementary Table S1.

147 **2.2 Isotope-enabled model simulations**



148 For this study, we performed a series of fully coupled paleoclimate simulations with the
149 iCESM1.2 (Brady et al., 2019), using a model resolution of approximately $1.9^\circ \times 2.5^\circ$ in the
150 atmosphere and land and $1^\circ \times 1^\circ$ in the ocean and sea ice, respectively, providing simulated
151 precipitation oxygen and hydrogen isotopes ($\delta^{18}\text{O}$ and $\delta^2\text{H}$) (Brady et al., 2019; Hu et al., 2019;
152 Tabor et al., 2018). We also combine simulated precipitation stable-isotope data to examine
153 precessional-scale variations in precipitation d-excess ($\delta^2\text{H} - 8 \times \delta^{18}\text{O}$) (Dansgaard, 1964). To
154 validate our iCESM1.2 present-day (iCESM-PD) simulations, we have used the available
155 IAEA Global Network of Isotopes in Precipitation (GNIP) datasets for the Asian domain
156 (Accessible at <https://nucleus.iaea.org/wiser>), published precipitation isotope records (Sinha et
157 al., 2019), and data from the isotopes-incorporated Global Spectral Model – isoGSM2
158 (Yoshimura et al., 2008).

159 First, we conducted an idealized transient simulation covering the orbital forcing history of the
160 past 130,000 years (iCESM-130ka), using fixed pre-industrial conditions of greenhouse gas
161 (GHG) concentrations, ice sheets, and bathymetry. The transient simulation employs an orbital
162 temporal acceleration (Lorenz and Lohmann, 2004a; Timmermann et al., 2007) factor of 100,
163 consistent with previous studies, which compresses the 130,000-year forcing history into 1,300
164 model years. The acceleration choice is justified by the fact that we focus here on atmospheric
165 processes primarily controlled by changes in land and ocean surface temperatures, with
166 adjustment timescales that are orders of magnitude faster than the precessional cycle forcing.
167 In our 130 ka-orbitally forced iCESM1.2 simulation, we analyzed the spatiotemporal patterns
168 of annual-mean anomalies of precipitation amount and $\delta^{18}\text{O}_p$. We further compared our
169 simulated precipitation patterns with the transient CESM1.2 simulation over the past three
170 million years (CESM-3Ma) (Timmermann et al., 2022; Yun et al., 2023), which was forced by
171 time-varying orbital, GHG, and realistic ice-sheet forcings. CESM-3Ma simulation uses a



172 lower horizontal resolution (3.75° in the atmosphere and 3° in the ocean), and an orbital
173 acceleration of only 5, but does not include isotopes.

174 Next, we performed model sensitivity experiments with iCESM1.2 to evaluate the equilibrium
175 climate responses to maximum (P_{\max}) and minimum (P_{\min}) precession conditions (iCESM- P_{\max}
176 and iCESM- P_{\min}). These 100-year-long fully coupled time-slice sensitivity experiments branch
177 off from year 900 of a 1,000-year-long iCESM-PD control experiment. The two idealized
178 simulations use a high eccentricity (Berger and Loutre, 1991) of 0.0493 to amplify the
179 precessional effects. The simulations reach a quasi-equilibrium state for important atmospheric
180 variables within 100 years. Much of our analysis from these two simulations is based on the
181 June-July-August (JJA) seasonal averages of the last 40 model years. Furthermore, we
182 compared iCESM P_{\min} and P_{\max} precipitation and circulation patterns with ultra-high-resolution
183 simulations ($1/4^\circ$ in the atmosphere and $1/10^\circ$ in the ocean) conducted for Marine Isotope
184 Stages (MIS)-5d (115 ka) and MIS-5e (125 ka) using the CESM1.2 (Chu et al., 2020; Huang
185 et al., 2021; Raavi et al., 2023; Wengel et al., 2021) (hiresCESM-5d and hiresCESM-5e). This
186 analysis provides further insights into the robustness of our results, enabling a more nuanced
187 characterization of regional aspects.

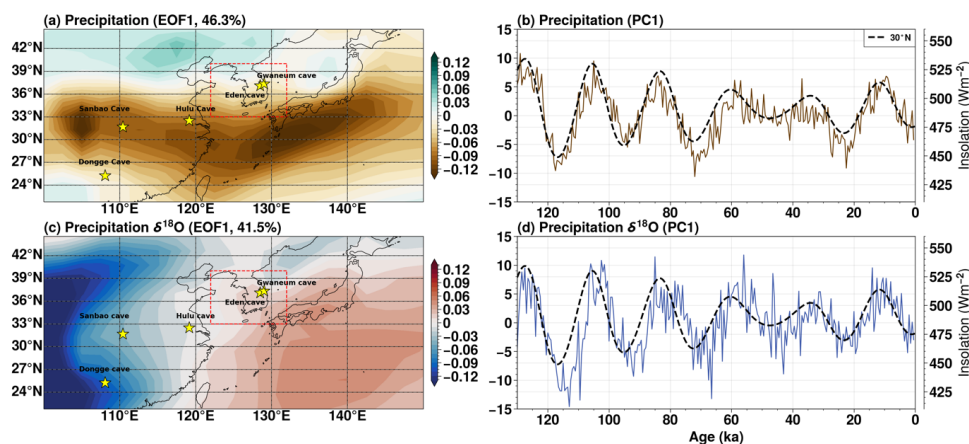
188 To quantify the KP precipitation and $\delta^{18}\text{O}_p$ responses to the P_{\min} and P_{\max} conditions, we
189 performed water-tagging experiments using the iCESM to track changes in source regions and
190 their relative contributions to the KP. The experiments were conducted using orbital
191 parameters corresponding to 124 ka (P_{\min}) and 119 ka (P_{\max}), along with current atmospheric
192 and oceanic conditions (including the initial isotopic composition) derived from the iCESM-
193 PD simulation. We tag a total of 14 boxes (7 each over land and Ocean), based on the major
194 contributors to the Asian region (Hu et al., 2019). The box latitude and longitude were chosen
195 following Wen et al. (2024), although we have excluded regions from the calculations with



196 minimal contribution ($< 10\%$) to the total rainfall and no effect on the anomalous $\delta^{18}\text{O}_p$. The
 197 regional pattern of the simulated $\delta^{18}\text{O}_p$ is determined by the $\delta^{18}\text{O}$ of the vapor from the tagged
 198 regions, followed by hydrological processes and rainout history (Tabor et al., 2018). Each
 199 tagging experiment was conducted over 40 model years, with the mean values from the last 20
 200 years (both summer and annual) used for analysis. Further information on the tagging
 201 experiment is provided in the supplementary material (Section S1).

202 3 Results and Discussion

203 3.1 Precipitation and $\delta^{18}\text{O}$: Model and Proxies



204

205 *Figure 1: First empirical orthogonal function (EOF1) and corresponding principal component*
 206 *(PC1) of annual mean precipitation (a, b) and precipitation- $\delta^{18}\text{O}$ (c, d) anomalies are*
 207 *calculated for Eastern Asia using the 130ka orbitally forced transient iCESM simulation.*
 208 *Korean caves and cave locations for the China composite record are marked by yellow stars in*
 209 *(a, c). A red dashed box marks the Korean Peninsula (KP) region. The black dashed curve in (b,*
 210 *d) represents summer insolation at 30°N.*

211 To extract the dominant modes of variability in Eastern Asia precipitation amount and $\delta^{18}\text{O}_p$
 212 from the transient iCESM-130ka simulation, we calculate the first Empirical Orthogonal
 213 Function (EOF1) and the corresponding principal component (PC1) time series for the selected
 214 Eastern Asian region ($22\text{--}45^\circ\text{N}$, $100\text{--}150^\circ\text{E}$), including eastern China, the KP, and Japan (Fig.



215 1). The leading EOF of annual mean precipitation variability exhibits a north-south dipole in
216 the selected EASM domain (Fig. 1a), characterized by strong precessional-scale variability and
217 correlating with the NHSI at 30°N (Fig. 1b). The precipitation anomalies associated with the
218 change in boreal summer insolation exhibit the strongest signal in an east-west elongated
219 structure between 25°N and 35°N. For northern-hemisphere summer perihelion conditions
220 (low precessional index), this area is characterized by anomalously dry conditions, whereas for
221 northern-hemisphere summer aphelion conditions (high precessional index), it is characterized
222 by anomalously wet conditions (Fig. S2). Most notably, Korea lies on the nodal line of the
223 precipitation dipole pattern, suggesting a weak annual-mean precession signal over the KP
224 (Fig. 1a). A similar precipitation pattern also emerges for the CESM-3Ma transient simulation
225 (Yun et al., 2023) over the study area (Fig. S3), indicating that the effects of GHGs and ice
226 sheet forcing are relatively minor in driving the EASM spatial precipitation patterns on
227 precession scales. However, in this case, the nodal line lies slightly south of the KP. The ultra-
228 high-resolution simulations confirm the overall large-scale response pattern in summer
229 precipitation to changes in the precessional index, albeit with somewhat drier conditions over
230 the KP, relative to the coarser-resolution CESM-3Ma and iCESM-130ka simulations (See
231 comparisons in Fig. S2).

232 Contrasting the meridional dipole in precipitation, the leading mode of $\delta^{18}\text{O}_p$ variability
233 exhibits an east-west (zonal) dipole pattern over our selected study region (Fig. 1c). The $\delta^{18}\text{O}_p$
234 dipole, which is characterized by relative ^{18}O -depletion (enrichment) for western (eastern) Asia
235 during northern hemisphere summer perihelion, has previously been presented as a notable
236 feature over the broader Asian summer monsoon region on precession scales (Wen et al., 2024).
237 In the western part of this dipole (China), we observe pronounced precessional-scale $\delta^{18}\text{O}_p$
238 signals; in the eastern part (Japan, Korea, and nearby seas), we generally find weaker variability
239 that is antiphase with the west (Fig. 1c and Fig. 1d). For the KP region, the simulated



240 precessional signal in $\delta^{18}\text{O}_p$ is strongly suppressed (similar to the rainfall pattern).

241 The near absence of precessional variability in hydroclimate predicted by the models can now

242 be tested using our speleothem isotope data from the KP (Fig. 2a). The Korean speleothem

243 stable carbon isotope ($\delta^{13}\text{C}_{sp}$) records correspond well with the Chinese $\delta^{18}\text{O}_{sp}$ records (blue

244 and gray curves, respectively, Fig. 2b), and the growth frequency of Korean speleothems

245 exhibits clear signals that correspond to orbital-scale hydrologic changes (Jo et al., 2014).

246 However, Korean $\delta^{18}\text{O}_{sp}$ records show no apparent precessional signal (red curves, Fig. 2b).

247 This observational result is consistent with the muted response in simulated $\delta^{18}\text{O}_p$ in the KP

248 region to precessional forcing (Fig. 1c). This raises the question of which physical processes

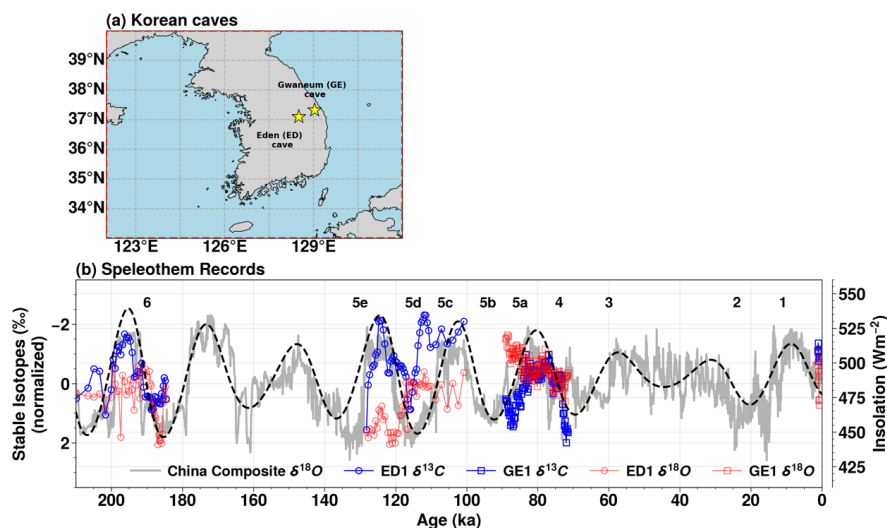
249 govern the $\delta^{13}\text{C}_{sp}$ on a precessional scale. Previous studies from the KP (Jo et al., 2010, 2011,

250 2014) suggested that precessional-scale changes in $\delta^{13}\text{C}_{sp}$ could be related to summer-

251 temperature and rainfall-driven anomalies in terrestrial productivity. However, a more detailed

252 investigation of the underlying processes driving precessional-scale variations in $\delta^{13}\text{C}_{sp}$ is

253 beyond the scope of our comprehensive water-isotope analysis of the KP.



254

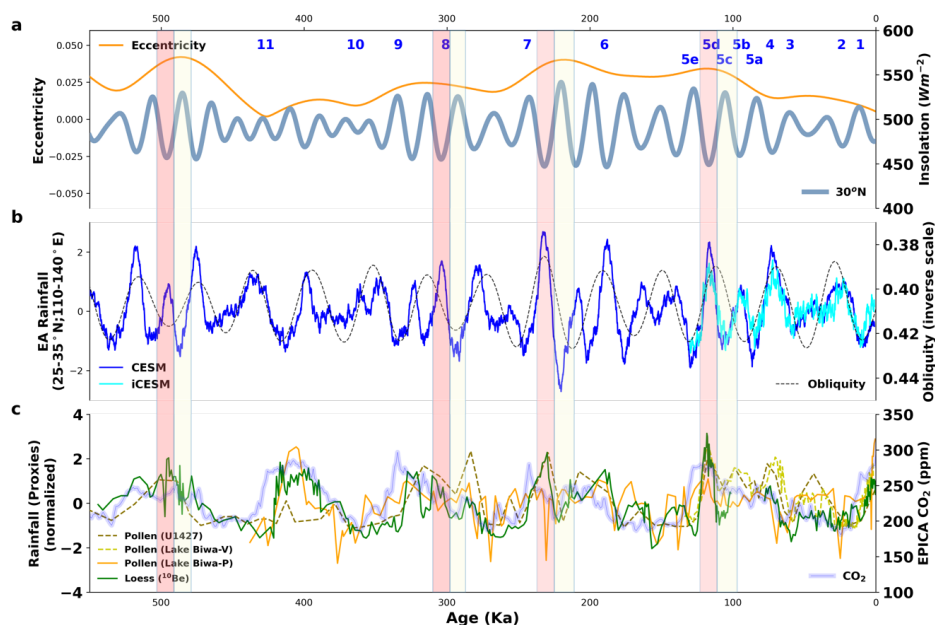
255 *Figure 2: Korean peninsula (red box, Figure 1) with Korea cave locations (a). Speleothem*

256 *records ($\delta^{13}\text{C}$ and $\delta^{18}\text{O}$) from Korean caves (Gwaneum (GE1) cave and Eden (ED1) cave) and*



257 *the Chinese caves composite record ($\delta^{18}O$) comparison (b). The marine isotope stage (MIS) is*
258 *indicated above the curves in (b). The black dashed curve in (b) represents summer insolation*
259 *at 30°N.*

260 According to the transient iCESM-130ka and CESM-3Ma simulations, precipitation over
261 Eastern Asia (Fig. 3b) exhibits precessional signals, which are out of phase with insolation. It
262 is important to note that simulated precessional scale precipitation suppresses during glacial
263 maxima in eastern Asia, documenting the influence of the 80-120 kyr eccentricity forcing on
264 the amplitude modulation of precession (Fig. 3a and Fig. 3b). There are several East Asian
265 hydroclimate proxies, such as ^{10}Be in loess from central China (Beck et al., 2018), pollen
266 records from Japan (Hayashi et al., 2017, 2021; Tarasov et al., 2011) (Fig. 3c), and total
267 nitrogen content in Lake Biwa (Iwamoto and Inouchi, 2007), which support and demonstrate
268 the above-mentioned features in regional-simulated precipitation. Speleothem records from
269 Japan (Kato et al., 2021; Mori et al., 2018) lack sufficient data points within the 0-130ka
270 simulated period, and the intermittent time span does not encompass high-insolation periods,
271 which would be necessary to validate the simulated isotopic composition. Some mismatches
272 between the pollen records and the model occur during MIS11 and low- CO_2 conditions,
273 suggesting that vegetation dynamics in the region may, in part, be driven directly by CO_2 , either
274 through temperature or the CO_2 fertilization effect. However, uncertainties in the chronology
275 of the palynological reconstruction preclude a definitive conclusion at this time. Moreover, the
276 simulations indicate a stronger 41ka obliquity signal, particularly during periods of low
277 eccentricity, which seems absent in the paleo proxy records (Fig. 3b).



278

279 **Figure 3:** Comparison of simulated Eastern Asian (EA) rainfall from the climate model
 280 simulations with prominent precipitation proxy records from the region over the last 550 ka.
 281 Summer Insolation (30 °N) and eccentricity (high eccentricity and low/high insolation
 282 highlighted with pink/yellow bars) (a). Rainfall (mm/day) from iCESM (this study) and CESM
 283 3Ma simulations, along with obliquity (b). Loess ¹⁰Be (central China) and EASM rainfall (Beck
 284 et al., 2018), along with CO₂ and palynological (Japan) rainfall reconstructions using the Lake
 285 Biwa pollen records (c). Lake Biwa-V (Hayashi et al., 2017) is based on vegetation response,
 286 and Lake Biwa-P (Tarasov et al., 2011) is based on the modern analogue technique. The marine
 287 isotope stage (MIS) is indicated above the top panel curves. For records' references, see Table
 288 S1. It should be noted that the Chinese ¹⁰Be record has been plotted after shifting the age by -
 289 6ka (see Section S2), which then aligns well with other regional proxies (c) and model-
 290 simulated precipitation (Fig. S4).

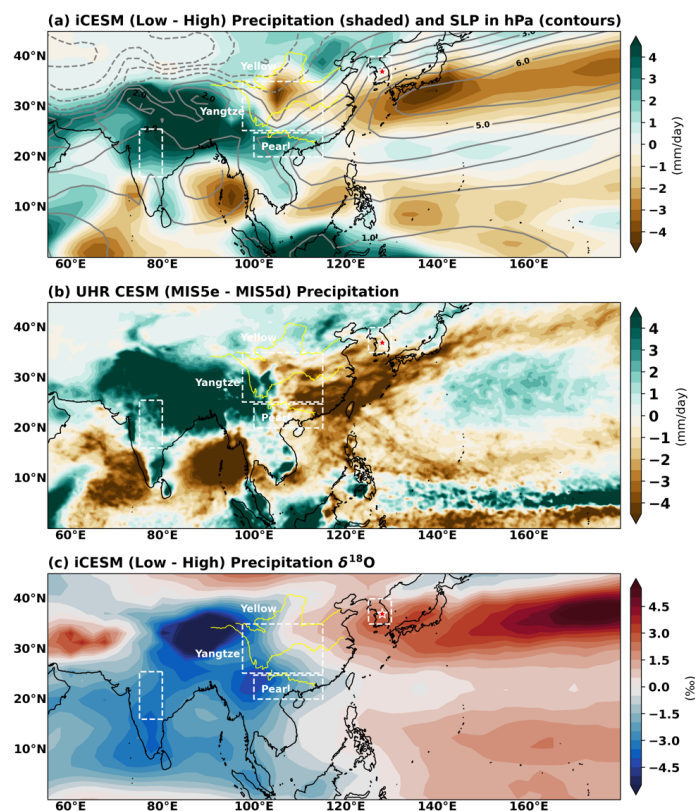
291

292 3.2 Precession versus EASM atmospheric circulation

293 As discussed in the previous section, under low precession conditions, a region of low
 294 precipitation in the eastern EASM domain zonally extends from KP across southern Japan into
 295 the central North Pacific. Our simulation shows that the region of low precipitation is co-
 296 located with an anomalously high sea level pressure (SLP; contour lines, Fig. 4a) and
 297 suppression of atmospheric convection (Fig. S5c, contour), in concordance with the
 298 intensification of the anomalous WNPSH (geopotential height, Fig. S5c). Supporting evidence



299 comes from an integrated moist static energy budget analysis by Wen et al. (2024), which
300 showed that the reduction in rainfall is linked to descending air motion. Our simulated
301 precipitation pattern, meridional and zonal wind components, and strength of anomalous
302 WNPSH are well supported by the difference of the hiresCESM-5e and hiresCESM-5d
303 experiments (Fig. 4b and Fig. S5), even though the anomalies over the KP are slightly stronger
304 compared to the ~2 degree resolution iCESM.



305

306 **Figure 4:** Difference between precession minimum (Low) and maximum (High). Composites of
307 summer mean precipitation (shaded) and sea level pressure (SLP, contour), from iCESM1.2 (a).
308 Same as (a) with CESM Ultra High Resolution (UHR) simulation for MIS5e and 5d (b), and
309 summer mean precipitation- $\delta^{18}\text{O}$, from iCESM1.2 (c). The dashed boxes shown are used to
310 extract 130 ka time series from the model simulations: India, central China, South China, and
311 Korea (left to right in increasing longitude order). The yellow curves on the map indicate major
312 rivers in China. The red star represents the Korean cave region.

313



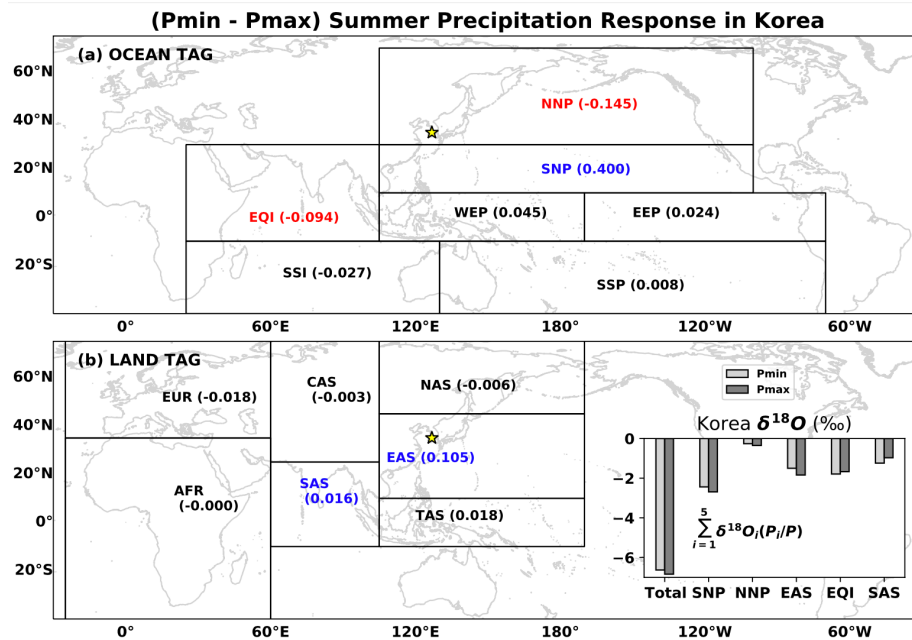
314 In addition, the simulated western branch of the anomalously strong WNPSH (Fig. S3a, d)
315 might help transport more moisture from the Pacific Ocean toward northern China and the
316 northern part of KP, resulting in regional positive precipitation anomalies in the model. The
317 rainfall pattern corresponds to an overall weakening and a slight northward shift of the Korean
318 and Japanese summer monsoon systems, specifically the Changma and Meiyu-Baiu fronts,
319 respectively. On the other hand, the KP hydroclimate reconstructed from speleothem proxies
320 (viz., growth frequency) suggests signals of a wetter climate during interglacial periods (Jo et
321 al., 2014), which are characterized by northern hemisphere summer perihelion. It is worth
322 noting that the Korean caves are primarily located in the mountainous Gangwon-do region of
323 South Korea and range in altitude (Jo et al., 2014). It is possible that orbital forcing may also
324 influence the precipitation intensity and the extent of the nodal line, relative to local
325 topographic features (Fig. 4b).

326 We further explored the mechanisms for the precessional muting of precipitation and $\delta^{18}\text{O}_p$ for
327 the KP and other parts along the nodal line, both for summer (JJA) and annual mean conditions.
328 Using the water-isotope tagging method, we estimated the contributions from different
329 moisture sources to precipitation and $\delta^{18}\text{O}_p$ at the KP in JJA (Fig. 5). The Pacific Ocean
330 transports more moisture to the KP region during the northern hemisphere summer perihelion
331 (Fig. 5a). This anomalous moisture predominantly originates from the subtropical North
332 Pacific (SNP, 0.40 mm/d) due to the strengthening and northwest shift of the NWPSH. Land
333 moisture (Fig. 5b) from the East Asia region also contributes to the anomalous P_{\min}
334 precipitation over the KP in JJA (EAS, 0.11 mm/d). However, during P_{\min} less moisture from
335 the northern North Pacific (NNP, -0.15 mm/d) and the equatorial Indian Ocean (EQI, -0.09
336 mm/d) arrives in KP, which compensates the increase with a small cumulative change in
337 summer precipitation of 0.28 mm/d as a result. The annual-mean KP precipitation anomaly



338 between $P_{\min} - P_{\max}$, shows only a small change, ranging from 0.023 (SNP) to -0.15 mm/d
339 (EAS) in terms of moisture contributions (Fig. S6, Table S2).

340 JJA $\delta^{18}\text{O}_p$ over the KP, will be determined both, by regional rainfall and water vapor transport
341 contributions from the different source regions. Using the tagging methods and calculating
342 summer precipitation-weighted $\delta^{18}\text{O}_p$ values (Sect. S1 and Table S2) at KP (inset, Figure 5),
343 we find that the moisture transported from the SNP oceanic region to the KP is anomalously
344 enriched in P_{\min} relative to P_{\max} (+0.22‰), with additional contributions also from EAS land
345 moisture ($P_{\min} - P_{\max} = +0.31\%$). However, the transport of moisture from the distant Indian
346 Ocean (EQI) and the land (SAS) regions shows a compensating effect (EQI + SAS = -0.38‰).
347 Combined the SNP and EAS effects (enrichment) and the EQI and SAS contributions
348 (depletion) result in a small net anomalous enrichment of $\delta^{18}\text{O}_p$ (+0.22 ‰) in JJA over KP
349 during P_{\min} . On annual timescales (inset, Fig. S6), the compensation is even more pronounced,
350 leading to a small net depletion of $\delta^{18}\text{O}_p$ over the KP region by -0.1‰ ($P_{\min} - P_{\max}$).
351 Furthermore, the tagging experiment reveals that, for annual means, the Indian region plays a
352 negligible role in precessional-scale changes in precipitation and $\delta^{18}\text{O}_p$ over the KP (Fig. S6,
353 Table S2).

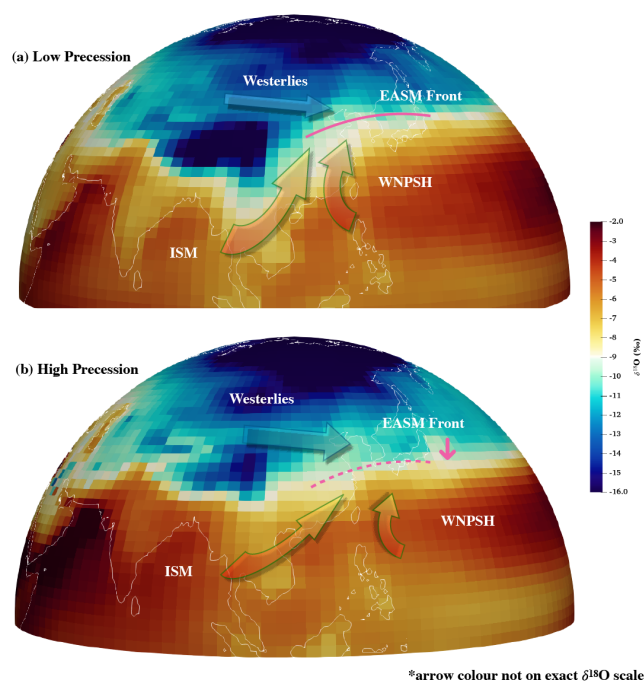


354
355

356 **Figure 5:** Differences in average summer (Jun-Aug) precipitation (mm/day) on the Korean
357 peninsula between P_{min} and P_{max} from various moisture sources over (a) ocean and (b) land.
358 Colored text refers to the major contributors (mean-state) to the Korean Peninsula (blue-
359 positive and red-negative for P_{min} - P_{max}), as shown in Table S2, which was considered in the
360 total calculations. Inset plot (lower right): the summer precipitation-weighted $\delta^{18}O$ in Korea
361 from major and nearby source contributors from Land (EAS, SAS) and the Ocean (SNP, NNP,
362 EQI). Korea is marked by a yellow star. See the supplementary material for the acronyms.

363

364 Overall, there is a tug-of-war between contributions from different oceanic and continental
365 regions to KP $\delta^{18}O_p$, leading to the muting of the precessional signal. For instance, the
366 anomalous WNPSH leads to a westward (eastward) shift of the ISM branch towards northern
367 China under low (high) precession conditions, as documented by an analysis of the vertically
368 integrated moisture transport (VIMT, Fig. S7). The schematic in Figure 6 summarizes these
369 findings by highlighting changes in circulation patterns and simulated $\delta^{18}O_p$ values for P_{min} and
370 P_{max} conditions.



371

*arrow colour not on exact $\delta^{18}O$ scale

372 *Figure 6: Schematics of precession effects on summer East Asian monsoon circulation and*
 373 *spatial distribution of precipitation- $\delta^{18}O$ (blue to dark orange: depleted (low $\delta^{18}O$) to enriched*
 374 *(high $\delta^{18}O$) in relative to low and high precession conditions). The thickness of the arrows*
 375 *represents the strength of the circulation systems. The solid and dashed pink lines indicate*
 376 *the location of the EASM front. (a) In the low precession case, ISM strengthening (a more southerly*
 377 *component), Westerlies (northward), and WNPSh (northwest) result in low (high) $\delta^{18}O_p$ over*
 378 *India to northern China (eastern Asia). The solid pink line indicates the EASM front location.*
 379 *(b) For the high precession case, the combined effects of the weakening of the ISM (more*
 380 *northeast component), the southward migration of the Westerlies, and the eastward*
 381 *movement of the WNPSh result in suppressed transport of Pacific moisture into the eastern*
 382 *domain of the EASM, result in high $\delta^{18}O_p$ across India to East Asia, however leading to*
 383 *relatively low $\delta^{18}O_p$ in eastern Asia. The interactions between two circulation systems (ISM*
 384 *and EASM) and the Westerlies create a nodal zone, which includes the Korean Peninsula (KP).*

385

386 Given the oceanic-continental moisture contributions to the orbital-scale characteristics of
 387 precessional-scale changes in KP hydroclimate, we anticipate that the dynamics will also be
 388 well captured in d-excess, which reflects the source region (Araguás-Araguás et al., 2000;
 389 Jouzel et al., 2013; Pfahl and Sodemann, 2014) and evaporative conditions (Masson-Delmotte
 390 et al., 2005; Uemura et al., 2008) of the moisture source. Like the d-excess seasonal variations,



391 to some extent, can serve as an analog for precessional changes, as precessional forcing
392 oftentimes modulates the amplitude of the seasonal signals in precipitation and isotopic
393 composition, due to the strength and position of atmospheric circulation (Bosmans et al., 2018).
394 As such, we examined d-excess variations on precessional timescales in our iCESM
395 simulations.

396 **3.3 Deuterium excess in simulations**

397 d-excess, a secondary parameter derived from stable water isotopic ratios, provides additional
398 insights into hydrological processes. Non-equilibrium conditions can lead to enrichment of ^2H
399 in the less stable phase (e.g., the gas phase) due to the higher diffusivity of hydrogen isotopes
400 relative to oxygen. For instance, during evaporation from the ocean surface, the strong gradient
401 in relative humidity accompanied by strong winds leads to higher d-excess in the vapor (Craig
402 and Gordon, 1965; Uemura et al., 2008). It has been suggested that climatic influences on
403 relative humidity, mediated by changes in atmospheric circulation, are captured in the d-excess
404 proxy in precipitation-based paleoarchives (Pfahl and Sodemann, 2014) (e.g., ice core,
405 speleothem). Studies have shown that the d-excess in paleowater can, in fact, be recovered
406 from speleothem fluid inclusion data (Held et al., 2025; Matthews et al., 2021).

407 The precipitation d-excess is sensitive to various hydrological processes between the “source”
408 and the “sink” (Xia et al., 2023), such as evaporation at the moisture source location (Craig and
409 Gordon, 1965; Merlivat and Jouzel, 1979), moisture recycling from the land (Gat, 1996; Gat et
410 al., 1994), raindrop evaporation (Risi et al., 2008; Stewart, 1975), and Rayleigh distillation
411 (Xia et al., 2023). On precessional timescales, one crucial parameter is the near-surface relative
412 humidity (R_{h_s}) at the source location. Over the tropical monsoon region, R_{h_s} changes may
413 occur mainly in conjunction with wind anomalies, as the annual mean surface temperature
414 changes are quite small on precession scales (Clement et al., 2004). We have analyzed the

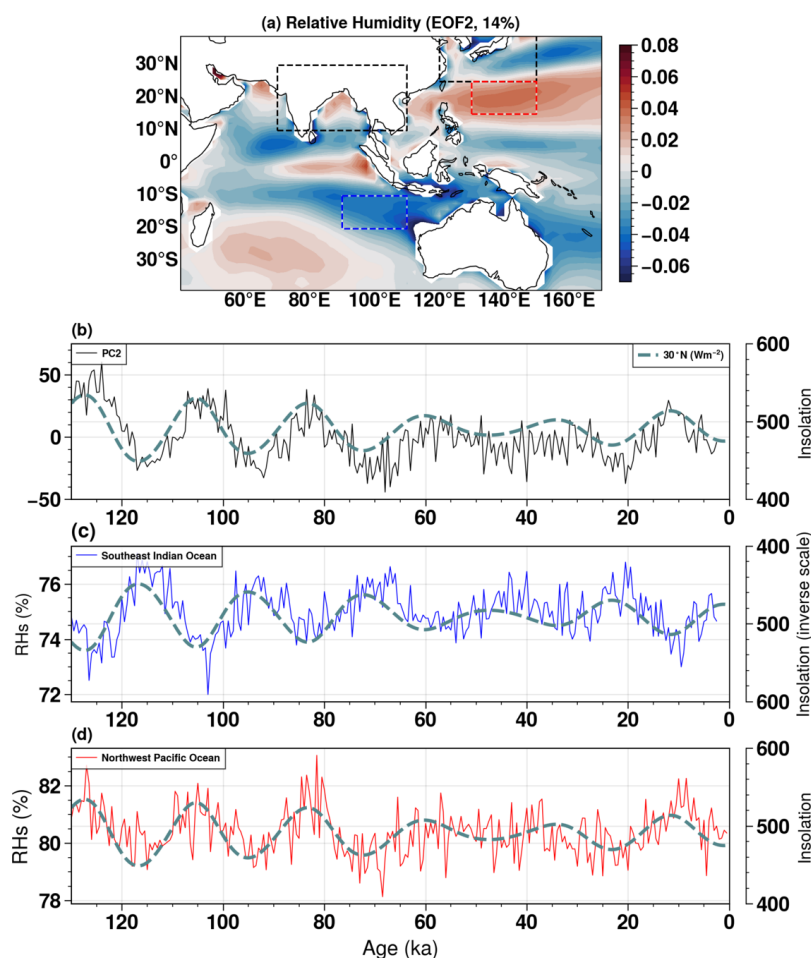


415 characteristics of simulated Rh_s at plausible source locations and d-excess variations at the
416 sinks. The spatial pattern and gradient of surface relative humidity over the Asian region are
417 reasonably well captured in the present-day simulation (Fig. S8). Brady et al. (2019) reported
418 that the d-excess values simulated by iCESM1 exhibit a positive median bias of 3.3‰ and a
419 poor correlation with GNIP observations. Our reinvestigation of simulated d-excess in the
420 Asian region for present-day conditions shows that GNIP and model data align reasonably well
421 (Fig. S9). A closer look at Fig. 4(b) in Brady et al. (2019) supports this conclusion. For the
422 Asian region, we found good agreement ($r = +0.52$, $p < 0.01$) between the annual mean d-
423 excess in GNIP observations and our iCESM-PD simulation (Fig. S10), with a smaller median
424 bias of +1.75‰, compared to the 3.3‰ global mean bias. Moreover, the strong seasonality in
425 the observed (GNIP) d-excess for East Asia, specifically for north and eastern Asian sites, is
426 well captured in iCESM-PD (Fig. S11), which is crucial in the current context because
427 precessional shifts are likely to influence the amplitude of the seasonal cycle, rather than the
428 annual mean.

429 To refine our interpretation of d-excess as a proxy for precessional signals over Asia, we further
430 investigate Rh_s variability in the Asian monsoon oceanic source domains, including the Indian
431 and Pacific Oceans. In the calculated EOFs for the Rh_s from the iCESM-130ka simulation,
432 EOF2 represents precessional-scale changes (Fig. 7). Over the southeast Indian Ocean and
433 northwest Pacific Ocean (rectangular boxes in Fig. 7), we observe strong precessional-scale
434 variability in Rh_s (Fig. 7b), with an amplitude change of approximately 3%-4% (Fig. 7c, d).
435 The chosen blue and red boxes, which exhibit strong out-of-phase variability (Fig. 7a),
436 respectively, closely correspond with the dominant moisture source regions to the South Asian
437 (Tabor et al., 2018) and Eastern Asian (Wen et al., 2024) monsoon regions under P_{\min} climate
438 (black dashed boxes, Fig. 7a). Subsequently, our results indicate that the South Asian and East
439 Asia (mainly Northeast China) continental domains also exhibit a substantial precessional-



440 scale variability in R_h_s (Fig. S12a, b), with an amplitude of about 10% change and in phase
 441 with the NHSI (Fig. S12c, d).



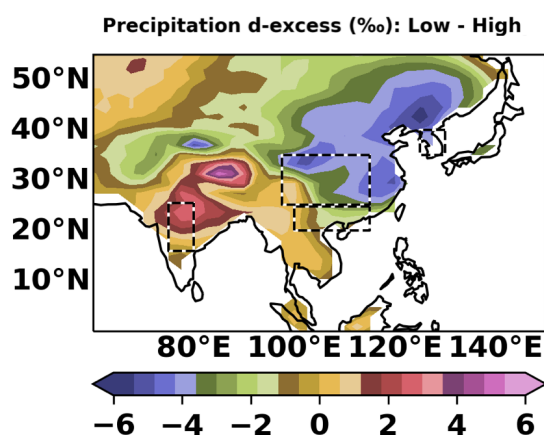
442

443 **Figure 7.** Second empirical orthogonal function (EOF2, a) and corresponding principal
 444 component (PC2, b) for the summer mean surface relative humidity for the 130ka transient
 445 simulation on iCESM1.2. Temporal evolution of surface relative humidity over oceanic source
 446 regions, Southeast Indian Ocean: blue curve (c) over blue dashed box (a); and Northwest
 447 Pacific Ocean: red curve (d) over red dashed box (a). The black dashed boxes represent the
 448 South Asian summer monsoon and the eastern extent of the EASM region (a). The dashed
 449 curve represents summer insolation at 30°N.

450 Moreover, our results show that the P_{\min} and P_{\max} conditions exhibit opposite signals in
 451 precipitation d-excess values between South Asia and East Asia (Fig. 8a). The d-excess is high



452 over India and low over central China for P_{min} . Specifically, in the KP, d-excess is low (high)
453 for high (low) NHSI. It should be noted that the KP d-excess differences for $P_{min} - P_{max}$ are
454 predominantly from the changes during the summer season; however, the Indian region's d-
455 excess values are higher throughout the year for P_{min} relative to P_{max} (Fig. S13). Our tagging
456 results also show that transported moisture from the Pacific Ocean and the East Asia
457 continental regions contributes to lower d-excess at KP under P_{min} conditions (Fig. S14), likely
458 due to relatively higher humidity over the source regions (Fig. 7d and Fig. S12d). To evaluate
459 the Rh_s and d-excess relationship quantitatively, the translation of the source region's Rh_s
460 change to the sink's precipitation d-excess has been estimated from the iCESM-130ka
461 simulation. A regional Rh_s regression on d-excess shows about a 0.3-0.4‰ increase in summer
462 precipitation d-excess values over South Asia with a 1% decrease in source region (southeast
463 Indian ocean) Rh_s (i.e., $\Delta(\text{d-excess})/\Delta Rh_s = \sim -0.4$) (Fig. S15a). And a 1% increase in Rh_s in
464 the northwest Pacific Ocean can cause a 0.7-0.8‰ decrease in summer precipitation d-excess
465 across Eastern Asia (i.e., $\Delta(\text{d-excess})/\Delta Rh_s = \sim -0.8$) (Fig. S15b).



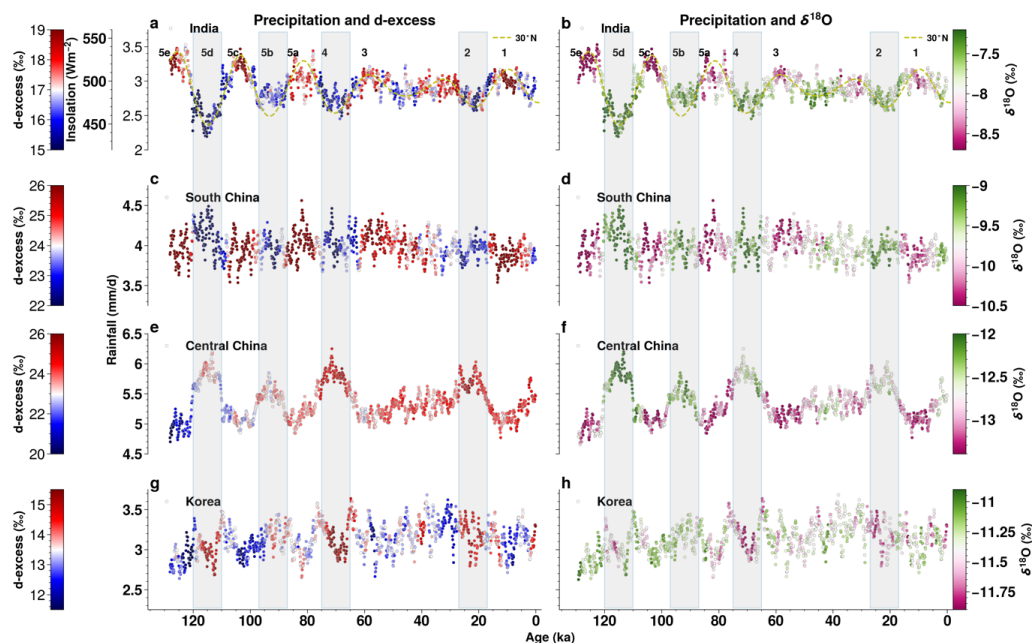
466

467 **Figure 8:** Precipitation d-excess for Low (P_{min}) - High (P_{max}) precession conditions. Black dashed
468 boxes represent regions: India, Central China, South China, and Korea (left to right), used to
469 extract the time series from the iCESM1.2 simulations.



470 **3.4 Pan-Asian monsoon context**

471 In this section, we refine our understanding of speleothem records from the KP in the broader
 472 context of hydroclimate changes across South to Eastern Asia in our transient simulation (Fig.
 473 S16). The iCESM-130ka simulation shows dominant anti-correlated precessional variability in
 474 precipitation between India (representative of Southern Asia) and central China (Fig. 9a and
 475 Fig. 9e). Furthermore, the amplitude of this variability is stronger (weaker) for high (low)
 476 eccentricity values, such as during MIS 5a-e and MIS3. On the other hand, precessional-scale
 477 variability in simulated KP precipitation, as well as in parts of southern China, is strongly
 478 muted (Fig. 9c and Fig. 9g), as discussed above. Moreover, over the KP, we found that
 479 precipitation exhibits an 11-kyr higher-order precessional harmonic, for instance, during MIS
 480 5d and MIS 4 (Fig. 9g). This signal likely arises from the nonlinearity of the moisture transport
 481 equation, which multiplies precessional-scale winds with precessional changes in moisture,
 482 leading to semi-precessional variability.



483



484 **Figure 9:** Simulated annual mean variations in precipitation (dots) for the last 130ka from an
485 orbital forced transient simulation conducted with iCESM1.2 for India (a,b), South China (c,d),
486 central China (e,f), and Korea (g,h) (see selected region boxes in Figure 8) in addition, colors
487 of dots show precipitation- $\delta^{18}O$ (pink to green, right panel) and d-excess (blue to red, left
488 panel) changes. Low insolation periods are marked by gray bars. The marine isotope stage
489 (MIS) is indicated above the top panel curves.

490

491 In the Indian region, apart from the strong precessional signals in precipitation, we see
492 precessional variability in d-excess and $\delta^{18}O_p$, with high (low) d-excess and depleted (enriched)
493 $\delta^{18}O_p$ values for high (low) insolation (Fig. 9a and Fig. 9b). Here, the change in d-excess values
494 is predominantly controlled by the surface conditions at the ISM moisture source region, that
495 is, high and low Rh_s values for low and high precession conditions, respectively, as discussed
496 above. In central China, $\delta^{18}O_p$ varies in phase with the anomalies over India (Fig. 9b and Fig.
497 9f). However, their d-excess variations are essentially anti-correlated (Fig. 9a and Fig. 9e), in
498 particular for MIS5e and 5c, reflecting the complex interplay between the Indian and Pacific
499 Ocean moisture sources and continental moisture effects. Our results support the previously
500 suggested role of the ISM branch in controlling precipitation isotopic ratios across China (see
501 supporting Fig. S4a and Fig. S4b). Furthermore, we observe that KP precipitation and $\delta^{18}O_p$
502 exhibit little precessional variability due to the compensating effects described above. In
503 contrast, d-excess over the KP shows a more pronounced precessional signal (Fig. 9g). This d-
504 excess variability responds to the balance between oceanic and continental moisture transport
505 and changes in the surface conditions of source regions (i.e., Rh_s) on precessional scales.
506 Moreover, the KP d-excess precessional-scale variability is a unique feature as compared to
507 other Eastern Asian regions, with high values occurring during MIS 5d, b, 4, and 2. The positive
508 feedback (kinetic effect) to the vapor d-excess could be even stronger for P_{max} relative to P_{min}
509 when dry/cold winds pass over the ocean (Yoshimura and Ichiyanagi, 2009) (e.g., the Yellow
510 Sea).

511



512 **4 Summary and concluding remarks**

513 Our study focuses on the muted precessional-scale hydroclimate variations in the KP region,
514 as observed in our transient climate model simulations and $\delta^{18}\text{O}_{\text{sp}}$ records from South Korean
515 caves. The muting of the $\delta^{18}\text{O}_{\text{p}}$ signal can be attributed to compensating effects between
516 oceanic and continental moisture sources. We further explored how the KP hydroclimate is
517 linked to large-scale pan-Asian atmospheric variability. Our study illustrates that even along
518 the nodal line of the oxygen isotope dipole pattern, where $\delta^{18}\text{O}_{\text{sp}}$ and the iCESM simulation
519 indicate weak precessional variability in $\delta^{18}\text{O}_{\text{p}}$, the d-excess may still contain important
520 precessional signals, which are associated with large-scale changes in Pacific, Indian, and
521 continental moisture source region conditions, driven by the precessional changes in the Asian
522 summer monsoon circulation and in the intensity of the WNPSH. Therefore, we advocate
523 validating model simulations using speleothem fluid inclusions (paleowater) to shed more light
524 on regional rainfall variability and large-scale atmospheric circulation changes across multiple
525 timescales, even in regions like the KP where oxygen isotope signals are muted.

526 Our simulations exhibit another interesting feature that has not previously been recognized:
527 simulated Korean precipitation shows evidence of semi-precessional hydroclimate variability.
528 A few studies have suggested that such semi-precessional signals may result from a response
529 to solar insolation in low latitudes, modulating the EASM. Other potential mechanisms include
530 combination tones of the moisture transport, emerging from the product between precessional
531 signals in specific humidity and atmospheric advection. However, the underlying mechanism
532 for the semi-precessional variability over the KP remains unclear and may require further
533 investigation.

534 The present study highlights the importance of a multi-proxy approach, utilizing additional
535 speleothem proxies, such as trace elements, $\delta^{13}\text{C}$, and growth rate or frequency, in conjunction



536 with fluid inclusions. These proxies, along with data from marine and lacustrine archives, may

537 provide further insights to help reconcile regional hydroclimatic records from the EASM region

538 and elucidate their underlying mechanisms.

539



540 **Acknowledgments:** N.S., A.T., S.L., D.C., and K.Y. received funding from the Institute for
541 Basic Science (IBS) under IBS-R028-D1. J.W. acknowledges funding from the Institute for
542 Basic Science under IBS-R028-Y2. K.N.J. would like to thank the Ministry of Education of
543 the Republic of Korea and the National Research Foundation of Korea (NRF-
544 2023R1A2C1006352) for partial funding support. The simulations were conducted on the
545 IBS/ICCP supercomputer “Aleph,” a 1.43 petaflops high-performance Cray XC50-LC Skylake
546 computing system with 18,720 processor cores, 9.59 PB of storage, and 43 PB of tap archive
547 space. We also acknowledge the support of KREONET. We thank Jiang Zhu, Jesse
548 Nusbaumer, Robert Tomas, and Jun Hu for their assistance in resolving issues with the
549 iCESM1.2 installation/simulations on Aleph. Dr. Ryoma Hayashi from the Lake Biwa
550 Museum, Japan, is acknowledged for providing lake data and engaging in insightful
551 discussions. The authors gratefully acknowledge discussions with Dr. Ji-Eun Kim from the IBS
552 Center for Climate Physics regarding precessional rainfall variability over China.

553 **Author contributions:** N.S. and A.T. conceived the study. K.N.J. provided the Korean
554 speleothem $\delta^{18}\text{O}$ records. N.S. performed the model simulations with S.-S.L. and K.-S.Y. on
555 Aleph. N.S. analyzed model data with inputs from A.T. and S.-S.L. N.S. prepared all figures,
556 interpreted the results with A.T., S.-S.L., and J.A.W., and wrote the first draft. Inputs from
557 A.T., D.M.C., J.A.W., and S.-S.L. improved the overall structure of the manuscript. All authors
558 reviewed the final manuscript.

559 **Data Availability:**

560 The Korean speleothem $\delta^{18}\text{O}$ record is included in the supplementary material (Table S3).

561 **Competing interests:**

562 The author(s) declare no competing interests.



563 **References**

- 564 Araguás-Araguás, L., Froehlich, K., and Rozanski, K.: Stable isotope composition of
565 precipitation over southeast Asia, *J. Geophys. Res.*, 103, 28721–28742,
566 <https://doi.org/10.1029/98JD02582>, 1998.
- 567 Araguás-Araguás, L., Froehlich, K., and Rozanski, K.: Deuterium and oxygen-18 isotope
568 composition of precipitation and atmospheric moisture, *Hydrol. Process.*, 14, 1341–1355,
569 [https://doi.org/10.1002/1099-1085\(20000615\)14:8%3C1341::AID-HYP983%3E3.0.CO;2-Z](https://doi.org/10.1002/1099-1085(20000615)14:8%3C1341::AID-HYP983%3E3.0.CO;2-Z),
570 2000.
- 571 Battisti, D. S., Ding, Q., and Roe, G. H.: Coherent pan-Asian climatic and isotopic response to
572 orbital forcing of tropical insolation, *J. Geophys. Res. Atmos.*, 119, 11,997–12,020,
573 <https://doi.org/10.1002/2014JD021960>, 2014.
- 574 Beck, J. W., Zhou, W., Li, C., Wu, Z., White, L., Xian, F., Kong, X., and An, Z.: A 550,000-year
575 record of East Asian monsoon rainfall from ¹⁰Be in loess, *Science*, 360, 877–881,
576 <https://doi.org/10.1126/science.aam5825>, 2018.
- 577 Berger, A. and Loutre, M. F.: Insolation values for the climate of the last 10 million years,
578 *Quaternary Science Reviews*, 10, 297–317, [https://doi.org/10.1016/0277-3791\(91\)90033-Q](https://doi.org/10.1016/0277-3791(91)90033-Q),
579 1991.
- 580 Bosmans, J. H. C., Erb, M. P., Dolan, A. M., Drijfhout, S. S., Tuenter, E., Hilgen, F. J., Edge, D.,
581 Pope, J. O., and Lourens, L. J.: Response of the Asian summer monsoons to idealized
582 precession and obliquity forcing in a set of GCMs, *Quaternary Science Reviews*, 188, 121–
583 135, <https://doi.org/10.1016/j.quascirev.2018.03.025>, 2018.
- 584 Brady, E., Stevenson, S., Bailey, D., Liu, Z., Noone, D., Nusbaumer, J., Otto-Bliesner, B. L.,
585 Tabor, C., Tomas, R., Wong, T., Zhang, J., and Zhu, J.: The Connected Isotopic Water Cycle in
586 the Community Earth System Model Version 1, *J Adv Model Earth Syst*, 11, 2547–2566,
587 <https://doi.org/10.1029/2019MS001663>, 2019.
- 588 Braun, K., Nehme, C., Pickering, R., Rogerson, M., and Scropton, N.: A Window into Africa’s
589 Past Hydroclimates: The SISAL_v1 Database Contribution, *Quaternary*, 2, 4,
590 <https://doi.org/10.3390/quat2010004>, 2019.
- 591 Cai, Y., Fung, I. Y., Edwards, R. L., An, Z., Cheng, H., Lee, J.-E., Tan, L., Shen, C.-C., Wang, X.,
592 Day, J. A., Zhou, W., Kelly, M. J., and Chiang, J. C. H.: Variability of stalagmite-inferred Indian
593 monsoon precipitation over the past 252,000 y, *Proc. Natl. Acad. Sci. U.S.A.*, 112, 2954–
594 2959, <https://doi.org/10.1073/pnas.1424035112>, 2015.
- 595 Chen, T.-J. G. and Chang, C.-P.: The Structure and Vorticity Budget of an Early Summer
596 Monsoon Trough (Mei-Yu) over Southeastern China and Japan, *Mon. Wea. Rev.*, 108, 942–
597 953, [https://doi.org/10.1175/1520-0493\(1980\)108%3C0942:TSAVBO%3E2.0.CO;2](https://doi.org/10.1175/1520-0493(1980)108%3C0942:TSAVBO%3E2.0.CO;2), 1980.
- 598 Cheng, H., Edwards, R. L., Broecker, W. S., Denton, G. H., Kong, X., Wang, Y., Zhang, R., and
599 Wang, X.: Ice Age Terminations, *Science*, 326, 248–252,
600 <https://doi.org/10.1126/science.1177840>, 2009.



- 601 Cheng, H., Edwards, R. L., Sinha, A., Spötl, C., Yi, L., Chen, S., Kelly, M., Kathayat, G., Wang,
602 X., Li, X., Kong, X., Wang, Y., Ning, Y., and Zhang, H.: The Asian monsoon over the past
603 640,000 years and ice age terminations, *Nature*, 534, 640–646,
604 <https://doi.org/10.1038/nature18591>, 2016.
- 605 Cheng, H., Zhang, H., Zhao, J., Li, H., Ning, Y., and Kathayat, G.: Chinese stalagmite
606 paleoclimate researches: A review and perspective, *Sci. China Earth Sci.*, 62, 1489–1513,
607 <https://doi.org/10.1007/s11430-019-9478-3>, 2019.
- 608 Cheng, H., Zhang, H., Cai, Y., Shi, Z., Yi, L., Deng, C., Hao, Q., Peng, Y., Sinha, A., Li, H., Zhao,
609 J., Tian, Y., Baker, J., and Perez-Mejias, C.: Orbital-scale Asian summer monsoon variations:
610 Paradox and exploration, *Sci. China Earth Sci.*, 64, 529–544,
611 <https://doi.org/10.1007/s11430-020-9720-y>, 2021.
- 612 Chiang, J. C. H., Fung, I. Y., Wu, C.-H., Cai, Y., Edman, J. P., Liu, Y., Day, J. A., Bhattacharya, T.,
613 Mondal, Y., and Labrousse, C. A.: Role of seasonal transitions and westerly jets in East Asian
614 paleoclimate, *Quaternary Science Reviews*, 108, 111–129,
615 <https://doi.org/10.1016/j.quascirev.2014.11.009>, 2015.
- 616 Chiang, J. C. H., Swenson, L. M., and Kong, W.: Role of seasonal transitions and the
617 westerlies in the interannual variability of the East Asian summer monsoon precipitation,
618 *Geophys. Res. Lett.*, 44, 3788–3795, <https://doi.org/10.1002/2017GL072739>, 2017.
- 619 Chu, J.-E., Lee, S.-S., Timmermann, A., Wengel, C., Stuecker, M. F., and Yamaguchi, R.:
620 Reduced tropical cyclone densities and ocean effects due to anthropogenic greenhouse
621 warming, *Sci. Adv.*, 6, eabd5109, <https://doi.org/10.1126/sciadv.abd5109>, 2020.
- 622 Clemens, S. C., Holbourn, A., Kubota, Y., Lee, K. E., Liu, Z., Chen, G., Nelson, A., and Fox-
623 Kemper, B.: Precession-band variance missing from East Asian monsoon runoff, *Nat*
624 *Commun*, 9, 3364, <https://doi.org/10.1038/s41467-018-05814-0>, 2018.
- 625 Clement, A. C., Hall, A., and Broccoli, A. J.: The importance of precessional signals in the
626 tropical climate, *Climate Dynamics*, 22, 327–341, [https://doi.org/10.1007/s00382-003-0375-](https://doi.org/10.1007/s00382-003-0375-8)
627 8, 2004.
- 628 Craig, H. and Gordon, L. I.: Deuterium and oxygen 18 variations in the ocean and marine
629 atmosphere, 1965.
- 630 Dai, G., Zhang, Z., Otterå, O. H., Langebroek, P. M., Yan, Q., and Zhang, R.: A Modeling Study
631 of the Tripole Pattern of East China Precipitation Over the Past 425 ka, *JGR Atmospheres*,
632 126, e2020JD033513, <https://doi.org/10.1029/2020JD033513>, 2021.
- 633 Dansgaard, W.: Stable isotopes in precipitation, *Tellus*, 16, 436–468,
634 <https://doi.org/10.1111/j.2153-3490.1964.tb00181.x>, 1964.
- 635 Ding, Y.: Seasonal March of The East-Asian Summer Monsoon, in: *World Scientific Series on*
636 *Asia-Pacific Weather and Climate*, vol. 02, World Scientific, 3–53,
637 https://doi.org/10.1142/9789812701411_0001, 2004.



- 638 Fairchild, I. J., Smith, C. L., Baker, A., Fuller, L., Spötl, C., Matthey, D., McDermott, F., and
639 E.I.M.F.: Modification and preservation of environmental signals in speleothems, *Earth-*
640 *Science Reviews*, 75, 105–153, <https://doi.org/10.1016/j.earscirev.2005.08.003>, 2006.
- 641 Gasse, F., Vidal, L., Develle, A.-L., and Van Campo, E.: Hydrological variability in the Northern
642 Levant: a 250 ka multi-proxy record from the Yammoûneh (Lebanon) sedimentary sequence,
643 *Clim. Past*, 7, 1261–1284, <https://doi.org/10.5194/cp-7-1261-2011>, 2011.
- 644 Gat, J. R.: Oxygen and hydrogen isotopes in the hydrologic cycle, *Annu. Rev. Earth Planet.*
645 *Sci.*, 24, 225–262, <https://doi.org/10.1146/annurev.earth.24.1.225>, 1996.
- 646 Gat, J. R., Bowser, C. J., and Kendall, C.: The contribution of evaporation from the Great
647 Lakes to the continental atmosphere: estimate based on stable isotope data, *Geophysical*
648 *Research Letters*, 21, 557–560, <https://doi.org/10.1029/94GL00069>, 1994.
- 649 Ha, K., Heo, K., Lee, S., Yun, K., and Jhun, J.: Variability in the East Asian Monsoon: a review,
650 *Meteorological Applications*, 19, 200–215, <https://doi.org/10.1002/met.1320>, 2012.
- 651 Hayashi, R., Takahara, H., Inouchi, Y., Takemura, K., and Igarashi, Y.: Vegetation and endemic
652 tree response to orbital-scale climate changes in the Japanese archipelago during the last
653 glacial–interglacial cycle based on pollen records from Lake Biwa, western Japan, *Review of*
654 *Palaeobotany and Palynology*, 241, 85–97, <https://doi.org/10.1016/j.revpalbo.2017.02.008>,
655 2017.
- 656 Hayashi, R., Sagawa, T., Irino, T., and Tada, R.: Orbital-scale vegetation-ocean-atmosphere
657 linkages in western Japan during the last 550 ka based on a pollen record from the IODP site
658 U1427 in the Japan Sea, *Quaternary Science Reviews*, 267, 107103,
659 <https://doi.org/10.1016/j.quascirev.2021.107103>, 2021.
- 660 He, C., Liu, Z., Otto-Bliesner, B. L., Brady, E. C., Zhu, C., Tomas, R., Clark, P. U., Zhu, J., Jahn,
661 A., Gu, S., Zhang, J., Nusbaumer, J., Noone, D., Cheng, H., Wang, Y., Yan, M., and Bao, Y.:
662 Hydroclimate footprint of pan-Asian monsoon water isotope during the last deglaciation,
663 *Sci. Adv.*, 7, eabe2611, <https://doi.org/10.1126/sciadv.abe2611>, 2021.
- 664 Held, F., Cheng, H., Edwards, R. L., Kipfer, T., Tüysüz, O., Koç, K., Affolter, S., and Fleitmann,
665 D.: Hydrological variability in the Black Sea region during the last 670,000 years recorded in
666 multi-proxy speleothem records from northern Türkiye, *Quaternary Science Reviews*, 367,
667 109534, <https://doi.org/10.1016/j.quascirev.2025.109534>, 2025.
- 668 Hu, J., Emile-Geay, J., Tabor, C., Nusbaumer, J., and Partin, J.: Deciphering Oxygen Isotope
669 Records From Chinese Speleothems With an Isotope-Enabled Climate Model,
670 *Paleoceanography and Paleoclimatology*, 34, 2098–2112,
671 <https://doi.org/10.1029/2019PA003741>, 2019.
- 672 Huang, L., Lee, S., and Timmermann, A.: Caspian Sea and Black Sea Response to Greenhouse
673 Warming in a High-Resolution Global Climate Model, *Geophys Res Lett*, 48,
674 <https://doi.org/10.1029/2020GL090270>, 2021.



- 675 Igarashi, Y. and Oba, T.: Fluctuations in the East Asian monsoon over the last 144ka in the
676 northwest Pacific based on a high-resolution pollen analysis of IMAGES core MD01-2421,
677 Quaternary Science Reviews, 25, 1447–1459,
678 <https://doi.org/10.1016/j.quascirev.2005.11.011>, 2006.
- 679 Iwamoto, N. and Inouchi, Y.: Reconstruction of millennial-scale variations in the East Asian
680 summer monsoon over the past 300 ka based on the total carbon content of sediment from
681 Lake Biwa, Japan, Environ Geol, 52, 1607–1616, [https://doi.org/10.1007/s00254-006-0606-](https://doi.org/10.1007/s00254-006-0606-5)
682 5, 2007.
- 683 Jo, K., Woo, K. S., Cheng, H., Edwards, L. R., Wang, Y., Kim, R., and Jiang, X.: Textural and
684 carbon isotopic evidence of monsoonal changes recorded in a composite-type speleothem
685 from Korea since MIS 5a, Quat. res., 74, 100–112,
686 <https://doi.org/10.1016/j.yqres.2010.04.005>, 2010.
- 687 Jo, K., Woo, K. S., Lim, H. S., Cheng, H., Edwards, R. L., Wang, Y., Jiang, X., Kim, R., Lee, J. I.,
688 Yoon, H. I., and Yoo, K.-C.: Holocene and Eemian climatic optima in the Korean Peninsula
689 based on textural and carbon isotopic records from the stalagmite of the Daeya Cave, South
690 Korea, Quaternary Science Reviews, 30, 1218–1231,
691 <https://doi.org/10.1016/j.quascirev.2011.02.012>, 2011.
- 692 Jo, K., Woo, K. S., Yi, S., Yang, D. Y., Lim, H. S., Wang, Y., Cheng, H., and Edwards, R. L.: Mid-
693 latitude interhemispheric hydrologic seesaw over the past 550,000 years, Nature, 508, 378–
694 382, <https://doi.org/10.1038/nature13076>, 2014.
- 695 Jo, K., Yi, S., Lee, J.-Y., Woo, K. S., Cheng, H., Edwards, L. R., and Kim, S.-T.: 1000-Year Quasi-
696 Periodicity of Weak Monsoon Events in Temperate Northeast Asia since the Mid-Holocene,
697 Scientific Reports, 7, 15196, <https://doi.org/10.1038/s41598-017-15566-4>, 2017.
- 698 Jouzel, J., Delaygue, G., Landais, A., Masson-Delmotte, V., Risi, C., and Vimeux, F.: Water
699 isotopes as tools to document oceanic sources of precipitation: Water Isotopes and
700 Precipitation Origin, Water Resour. Res., 49, 7469–7486,
701 <https://doi.org/10.1002/2013WR013508>, 2013.
- 702 Jung, Y.-Y., Shin, W.-J., Seo, K.-H., Koh, D.-C., Ko, K.-S., and Lee, K.-S.: Spatial distributions of
703 oxygen and hydrogen isotopes in multi-level groundwater across South Korea: A case study
704 of mountainous regions, Science of The Total Environment, 812, 151428,
705 <https://doi.org/10.1016/j.scitotenv.2021.151428>, 2022.
- 706 Kathayat, G., Cheng, H., Sinha, A., Spötl, C., Edwards, R. L., Zhang, H., Li, X., Yi, L., Ning, Y.,
707 Cai, Y., Lui, W. L., and Breitenbach, S. F. M.: Indian monsoon variability on millennial-orbital
708 timescales, Sci Rep, 6, 24374, <https://doi.org/10.1038/srep24374>, 2016.
- 709 Kato, H., Amekawa, S., Hori, M., Shen, C.-C., Kuwahara, Y., Senda, R., and Kano, A.:
710 “Influences of temperature and the meteoric water $\delta^{18}\text{O}$ value on a stalagmite record in
711 the last deglacial to middle Holocene period from southwestern Japan,” Quaternary Science
712 Reviews, 253, 106746, <https://doi.org/10.1016/j.quascirev.2020.106746>, 2021.



- 713 Kim, S., Han, Y., Hur, S. D., Yoshimura, K., and Lee, J.: Relating Moisture Transport to Stable
714 Water Vapor Isotopic Variations of Ambient Wintertime along the Western Coast of Korea,
715 *Atmosphere*, 10, 806, <https://doi.org/10.3390/atmos10120806>, 2019.
- 716 Kutzbach, J. E., Liu, X., Liu, Z., and Chen, G.: Simulation of the evolutionary response of
717 global summer monsoons to orbital forcing over the past 280,000 years, *Clim Dyn*, 30, 567–
718 579, <https://doi.org/10.1007/s00382-007-0308-z>, 2008.
- 719 Lachniet, M. S.: Climatic and environmental controls on speleothem oxygen-isotope values,
720 *Quaternary Science Reviews*, 28, 412–432, <https://doi.org/10.1016/j.quascirev.2008.10.021>,
721 2009.
- 722 Lee, K.S., Woo, N.C., and Kim, K.: Factors controlling stable isotope composition of
723 precipitation in Northeast Asia, *JGSK*, 37, 183–192, 2001.
- 724 Li, X., Zhou, Y., Han, Z., Yuan, X., Yi, S., Zeng, Y., Qin, L., Lu, M., and Lu, H.: Loess deposits in
725 the low latitudes of East Asia reveal the ~20-kyr precipitation cycle, *Nat Commun*, 15, 1023,
726 <https://doi.org/10.1038/s41467-024-45379-9>, 2024.
- 727 Lin, F., Zhang, Q., Sinha, A., Wang, Z., Axelsson, J., Chen, L., Wang, T., and Tan, L.: Seasonal
728 to decadal variations of precipitation oxygen isotopes in northern China linked to the
729 moisture source, *npj Clim Atmos Sci*, 7, 14, <https://doi.org/10.1038/s41612-024-00564-x>,
730 2024.
- 731 Liu, X., Xie, X., Guo, Z., Yin, Z.-Y., and Chen, G.: Model-based orbital-scale precipitation $\delta^{18}\text{O}$
732 variations and distinct mechanisms in Asian monsoon and arid regions, *National Science*
733 *Review*, 9, nwac182, <https://doi.org/10.1093/nsr/nwac182>, 2022.
- 734 Liu, Z., Wen, X., Brady, E. C., Otto-Bliesner, B., Yu, G., Lu, H., Cheng, H., Wang, Y., Zheng, W.,
735 Ding, Y., Edwards, R. L., Cheng, J., Liu, W., and Yang, H.: Chinese cave records and the East
736 Asia Summer Monsoon, *Quaternary Science Reviews*, 83, 115–128,
737 <https://doi.org/10.1016/j.quascirev.2013.10.021>, 2014.
- 738 Lorenz, S. J. and Lohmann, G.: Acceleration technique for Milankovitch type forcing in a
739 coupled atmosphere-ocean circulation model: method and application for the Holocene,
740 *Climate Dynamics*, 23, 727–743, <https://doi.org/10.1007/s00382-004-0469-y>, 2004a.
- 741 Lorenz, S. J. and Lohmann, G.: Acceleration technique for Milankovitch type forcing in a
742 coupled atmosphere-ocean circulation model: method and application for the Holocene,
743 *Climate Dynamics*, 23, 727–743, <https://doi.org/10.1007/s00382-004-0469-y>, 2004b.
- 744 Maher, B. A. and Thompson, R.: Oxygen isotopes from Chinese caves: records not of
745 monsoon rainfall but of circulation regime, *J Quaternary Science*, 27, 615–624,
746 <https://doi.org/10.1002/jqs.2553>, 2012.
- 747 Masson-Delmotte, V., Jouzel, J., Landais, A., Stievenard, M., Johnsen, S. J., White, J. W. C.,
748 Werner, M., Sveinbjornsdottir, A., and Fuhrer, K.: GRIP Deuterium Excess Reveals Rapid and
749 Orbital-Scale Changes in Greenland Moisture Origin, *Science*, 309, 118–121,
750 <https://doi.org/10.1126/science.1108575>, 2005.



- 751 Matthews, A., Affek, H. P., Ayalon, A., Vonnhof, H. B., and Bar-Matthews, M.: Eastern
752 Mediterranean climate change deduced from the Soreq Cave fluid inclusion stable isotopes
753 and carbonate clumped isotopes record of the last 160 ka, *Quaternary Science Reviews*,
754 272, 107223, <https://doi.org/10.1016/j.quascirev.2021.107223>, 2021.
- 755 Merlivat, L. and Jouzel, J.: Global climatic interpretation of the deuterium-oxygen 18
756 relationship for precipitation, *J. Geophys. Res.*, 84, 5029,
757 <https://doi.org/10.1029/JC084iC08p05029>, 1979.
- 758 Mori, T., Kashiwagi, K., Amekawa, S., Kato, H., Okumura, T., Takashima, C., Wu, C.-C., Shen,
759 C.-C., Quade, J., and Kano, A.: Temperature and seawater isotopic controls on two
760 stalagmite records since 83 ka from maritime Japan, *Quaternary Science Reviews*, 192, 47–
761 58, <https://doi.org/10.1016/j.quascirev.2018.05.024>, 2018.
- 762 Park, Y., Lee, K.S., and Yu, J.Y.: Seasonal variations of dissolved ions and oxygen and
763 hydrogen isotopic compositions of precipitation in Chuncheon, Korea, *JGSK*, 42, 283–292,
764 2006.
- 765 Pfahl, S. and Sodemann, H.: What controls deuterium excess in global precipitation?, *Clim.*
766 *Past*, 10, 771–781, <https://doi.org/10.5194/cp-10-771-2014>, 2014.
- 767 Raavi, P. H., Chu, J.-E., Timmermann, A., Lee, S.-S., and Walsh, K. J. E.: Moisture control of
768 tropical cyclones in high-resolution simulations of paleoclimate and future climate, *Nat*
769 *Commun*, 14, 6426, <https://doi.org/10.1038/s41467-023-42033-8>, 2023.
- 770 Risi, C., Bony, S., and Vimeux, F.: Influence of convective processes on the isotopic
771 composition ($\delta^{18}\text{O}$ and δD) of precipitation and water vapor in the tropics: 2. Physical
772 interpretation of the amount effect, *J. Geophys. Res.*, 113, 2008JD009943,
773 <https://doi.org/10.1029/2008JD009943>, 2008.
- 774 Sinha, N., Chakraborty, S., and Mohan, P. M.: Modern rain-isotope data from Indian island
775 and the mainland on the daily scale for the summer monsoon season, *Data in Brief*, 23,
776 103793, <https://doi.org/10.1016/j.dib.2019.103793>, 2019.
- 777 Stewart, M. K.: Stable isotope fractionation due to evaporation and isotopic exchange of
778 falling waterdrops: Applications to atmospheric processes and evaporation of lakes, *J.*
779 *Geophys. Res.*, 80, 1133–1146, <https://doi.org/10.1029/JC080i009p01133>, 1975.
- 780 Sun, J. and Huang, X.: Half-precessional cycles recorded in Chinese loess: response to low-
781 latitude insolation forcing during the Last Interglaciation, *Quaternary Science Reviews*, 25,
782 1065–1072, <https://doi.org/10.1016/j.quascirev.2005.08.004>, 2006.
- 783 Sun, Y., Clemens, S. C., An, Z., and Yu, Z.: Astronomical timescale and palaeoclimatic
784 implication of stacked 3.6-Myr monsoon records from the Chinese Loess Plateau,
785 *Quaternary Science Reviews*, 25, 33–48, <https://doi.org/10.1016/j.quascirev.2005.07.005>,
786 2006.
- 787 Tabor, C. R., Otto-Bliesner, B. L., Brady, E. C., Nusbaumer, J., Zhu, J., Erb, M. P., Wong, T. E.,
788 Liu, Z., and Noone, D.: Interpreting Precession-Driven $\delta^{18}\text{O}$ Variability in the South Asian



- 789 Monsoon Region, *J. Geophys. Res. Atmos.*, **123**, 5927–5946,
790 <https://doi.org/10.1029/2018JD028424>, 2018.
- 791 Tarasov, P. E., Nakagawa, T., Demske, D., Österle, H., Igarashi, Y., Kitagawa, J., Mokhova, L.,
792 Bazarova, V., Okuda, M., Gotanda, K., Miyoshi, N., Fujiki, T., Takemura, K., Yonenobu, H., and
793 Fleck, A.: Progress in the reconstruction of Quaternary climate dynamics in the Northwest
794 Pacific: A new modern analogue reference dataset and its application to the 430-kyr pollen
795 record from Lake Biwa, *Earth-Science Reviews*, **108**, 64–79,
796 <https://doi.org/10.1016/j.earscirev.2011.06.002>, 2011.
- 797 Timmermann, A., Lorenz, S. J., An, S.-I., Clement, A., and Xie, S.-P.: The Effect of Orbital
798 Forcing on the Mean Climate and Variability of the Tropical Pacific, *Journal of Climate*, **20**,
799 4147–4159, <https://doi.org/10.1175/JCLI4240.1>, 2007.
- 800 Timmermann, A., Yun, K.-S., Raia, P., Ruan, J., Mondanaro, A., Zeller, E., Zollikofer, C., Ponce
801 de León, M., Lemmon, D., Willeit, M., and Ganopolski, A.: Climate effects on archaic human
802 habitats and species successions, *Nature*, **604**, 495–501, <https://doi.org/10.1038/s41586-022-04600-9>, 2022.
- 804 Uemura, R., Matsui, Y., Yoshimura, K., Motoyama, H., and Yoshida, N.: Evidence of
805 deuterium excess in water vapor as an indicator of ocean surface conditions, *J. Geophys.*
806 *Res.*, **113**, D19114, <https://doi.org/10.1029/2008JD010209>, 2008.
- 807 Volonté, A., Turner, A. G., Schiemann, R., Vidale, P. L., and Klingaman, N. P.: Characterising
808 the interaction of tropical and extratropical air masses controlling East Asian summer
809 monsoon progression using a novel frontal detection approach, *Weather Clim. Dynam.*, **3**,
810 575–599, <https://doi.org/10.5194/wcd-3-575-2022>, 2022.
- 811 Wang, B. and Lin: Rainy Season of the Asian–Pacific Summer Monsoon, *J. Climate*, **15**, 386–
812 398, [https://doi.org/10.1175/1520-0442\(2002\)015%3C0386:RSOTAP%3E2.0.CO;2](https://doi.org/10.1175/1520-0442(2002)015%3C0386:RSOTAP%3E2.0.CO;2), 2002.
- 813 Wang, B., Wu, Z., Li, J., Liu, J., Chang, C.-P., Ding, Y., and Wu, G.: How to Measure the
814 Strength of the East Asian Summer Monsoon, *Journal of Climate*, **21**, 4449–4463,
815 <https://doi.org/10.1175/2008JCLI2183.1>, 2008.
- 816 Wang, Y. J., Cheng, H., Edwards, R. L., An, Z. S., Wu, J. Y., Shen, C.-C., and Dorale, J. A.: A
817 High-Resolution Absolute-Dated Late Pleistocene Monsoon Record from Hulu Cave, China,
818 *Science*, **294**, 2345–2348, <https://doi.org/10.1126/science.1064618>, 2001.
- 819 Wen, Q., Liu, Z., Jing, Z., Clemens, S. C., Wang, Y., Yan, M., Ning, L., and Liu, J.: Grand dipole
820 response of Asian summer monsoon to orbital forcing, *npj Clim Atmos Sci*, **7**, 202,
821 <https://doi.org/10.1038/s41612-024-00749-4>, 2024.
- 822 Wengel, C., Lee, S.-S., Stuecker, M. F., Timmermann, A., Chu, J.-E., and Schloesser, F.: Future
823 high-resolution El Niño/Southern Oscillation dynamics, *Nature Climate Change*, **11**, 758–765,
824 <https://doi.org/10.1038/s41558-021-01132-4>, 2021.
- 825 Wu, C.-H., Lee, S.-Y., and Chiang, J. C. H.: Relative influence of precession and obliquity in
826 the early Holocene: Topographic modulation of subtropical seasonality during the Asian



- 827 summer monsoon, *Quaternary Science Reviews*, 191, 238–255,
828 <https://doi.org/10.1016/j.quascirev.2018.05.021>, 2018.
- 829 Xia, Z., Surma, J., and Winnick, M. J.: The response and sensitivity of deuterium and 17O
830 excess parameters in precipitation to hydroclimate processes, *Earth-Science Reviews*, 242,
831 104432, <https://doi.org/10.1016/j.earscirev.2023.104432>, 2023.
- 832 Xie, X., Liu, X., Chen, G., and Korty, R. L.: A Transient Modeling Study of the Latitude
833 Dependence of East Asian Winter Monsoon Variations on Orbital Timescales, *Geophysical
834 Research Letters*, 46, 7565–7573, <https://doi.org/10.1029/2019GL083060>, 2019.
- 835 Xue, G., Cai, Y., Zheng, Y., Zhang, H., Han, T., Huang, S., Cheng, X., Ma, L., Liu, C., Edwards, R.
836 L., Cheng, H., and Yan, H.: Western Pacific Subtropical High Modulates Regional
837 Hydroclimate Changes on Multiple Timescales Over Central China, *JGR Atmospheres*, 130,
838 e2024JD042735, <https://doi.org/10.1029/2024JD042735>, 2025.
- 839 Yang, H., Chou, Y.-M., Jiang, X., Zheng, W., He, Y., Banerjee, Y., Shen, C.-C., Yu, T.-L., Zhong,
840 Y., Humbert, F., and Liu, Q.: Chinese stalagmite $\delta^{18}\text{O}$ records reveal the diverse moisture
841 trajectories during the middle to late last glacial period, *Geol. Mag.*, 1–13,
842 <https://doi.org/10.1017/S0016756824000013>, 2024.
- 843 Yoshimura, K. and Ichiyangi, K.: A reconsideration of Seasonal Variation in Precipitation
844 Deuterium Excess Over East Asia, *J. Japan Soc. Hydrol. and Water Resour.*, 22, 262–276,
845 <https://doi.org/10.3178/jjshwr.22.262>, 2009.
- 846 Yoshimura, K., Kanamitsu, M., Noone, D., and Oki, T.: Historical isotope simulation using
847 Reanalysis atmospheric data, *J. Geophys. Res.*, 113, D19108,
848 <https://doi.org/10.1029/2008JD010074>, 2008.
- 849 Yun, K.-S., Timmermann, A., Lee, S.-S., Willeit, M., Ganopolski, A., and Jadhav, J.: A transient
850 coupled general circulation model (CGCM) simulation of the past 3 million years, *Clim. Past*,
851 19, 1951–1974, <https://doi.org/10.5194/cp-19-1951-2023>, 2023.
- 852 Zeller, E., Timmermann, A., Yun, K.-S., Raia, P., Stein, K., and Ruan, J.: Human adaptation to
853 diverse biomes over the past 3 million years, *Science*, 380, 604–608,
854 <https://doi.org/10.1126/science.abq1288>, 2023.
- 855 Zhang, H., Griffiths, M. L., Chiang, J. C. H., Kong, W., Wu, S., Atwood, A., Huang, J., Cheng, H.,
856 Ning, Y., and Xie, S.: East Asian hydroclimate modulated by the position of the westerlies
857 during Termination I, *Science*, 362, 580–583, <https://doi.org/10.1126/science.aat9393>,
858 2018.
- 859 Zhao, L., Xiao, H., Zhou, M., Cheng, G., Wang, L., Yin, L., and Ren, J.: Factors controlling
860 spatial and seasonal distributions of precipitation $\delta^{18}\text{O}$ in China, *Hydrological Processes*, 26,
861 143–152, <https://doi.org/10.1002/hyp.8118>, 2012.
- 862 Zheng, Y., Liu, H., Yang, H., Wang, H., Zhao, W., Zhang, Z., Huang, M., and Liu, W.: Decoupled
863 Asian monsoon intensity and precipitation during glacial-interglacial transitions on the

<https://doi.org/10.5194/egusphere-2026-3348>

Preprint. Discussion started: 19 June 2026

© Author(s) 2026. CC BY 4.0 License.



864 Chinese Loess Plateau, Nat Commun, 13, 5397, [https://doi.org/10.1038/s41467-022-33105-](https://doi.org/10.1038/s41467-022-33105-2)
865 2, 2022.

866 Zhu, H., Zhu, L., Luo, L., and Li, J.: Seasonal Variations of Modern Precipitation Stable
867 Isotopes over the North Tibetan Plateau and Their Influencing Factors, Water, 16, 150,
868 <https://doi.org/10.3390/w16010150>, 2023.

869